X. PLASMA PHYSICS*

Prof. S. C. Brown	C. D. Buntschuh	J. C. Ingraham
Prof. W. P. Allis	J. F. Clarke	J. J. McCarthy
Prof. G. Bekefi	J. D. Coccoli	W. J. Mulligan
Prof. S. Gruber	F. X. Crist	J. J. Nolan, Jr.
Prof. D. R. Whitehouse	E. W. Fitzgerald, Jr.	G. L. Rogoff
V. Arunasalam	W. H. Glenn, Jr.	R. E. Whitney

A. VELOCITY DISTRIBUTION MEASUREMENTS

The experimental apparatus for the measurement of the longitudinal velocity distribution has been completed and tested for the required properties. Basically, the velocity distribution is measured by the observation of the cyclotron radiation from individual electrons (that is, in the transparent limit) at two axially separated positions in the positive column of a dc discharge. The crosscorrelation function of the radiation at these two positions is then proportional to the axial velocity distribution with the velocity scale being the separation distance divided by the time scale of the crosscorrelation function.

The existence of collisions imposes some restrictions on the dimensions of the system. It is necessary to restrict the size of the plasma that is observed at each of the axial positions so that the ratio of the length of observation at one position to the distance between the positions is small. This limitation allows the "window" on the velocity distribution to be a small fraction of the velocity that is being measured. The separation between the two observation ports is restricted to be somewhat less than a mean-free path for elastic electronic collisions because the technique of measuring the crosscorrelation function requires that the radiation from each individual electron at one position be coherent with itself when it reaches the second position. The coherence is preserved only if the electron does not collide during its flight along the magnetic field from one position to the other. The error in the measurements resulting from these unwanted collisions could, in theory, be corrected for by knowing the probability of collision as a function of velocity. Fig. X-1 is the schematic representation of the technique of measurement. Furthermore, if one were to call the radiation by one electron into the waveguide nearest the cathode $S_2(t)$, then, if the electron reaches the waveguide nearest the anode without colliding, the signal received at this position, $S_1(t)$, would be just $S_2(t-d/v_1)$, where d is the waveguide separation, and v_1 is the electron's velocity along

*This work was supported in part by the U.S. Atomic Energy Commission under Contract AT(30-1)-1842; in part by the U.S. Air Force (Electronic Systems Division) under Contract AF19(604)-5992; and in part by the National Science Foundation under Grant G-9330.

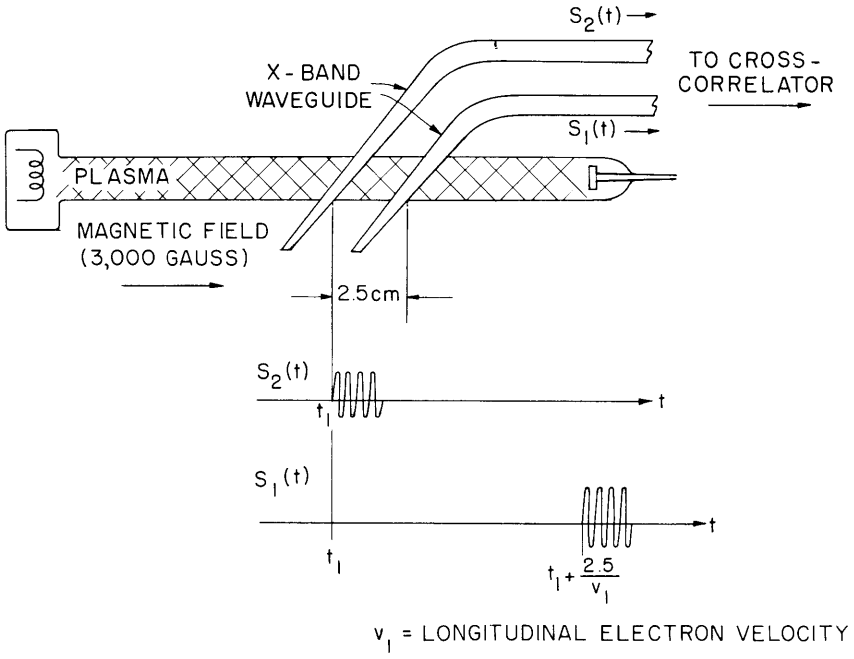

Fig. X-1. Schematic representation of measurement technique.

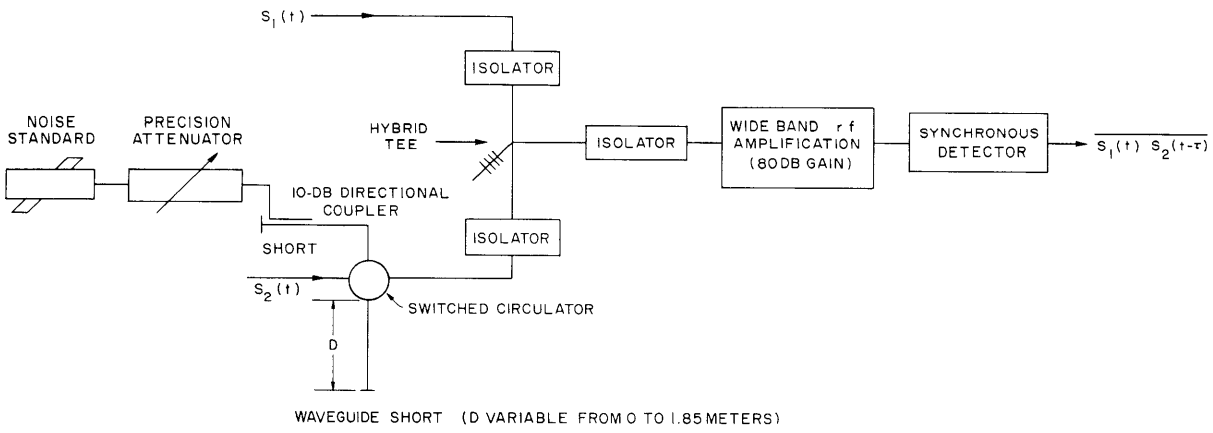

Fig. X-2. X-band crosscorrelator.

the magnetic field toward the anode of the discharge. One sees that simply by delaying $S_2(t)$ by the time τ, the power in the product $[S_1(t)][S_2(t-\tau)]$ is equal to the power radiated by each electron times the number of electrons proceeding longitudinally with velocity d/τ (within some uncertainty of velocity caused by the nonzero time duration within the waveguides). Figure X-2 is a block diagram of the equipment required to make the mathematical manipulations indicated above.

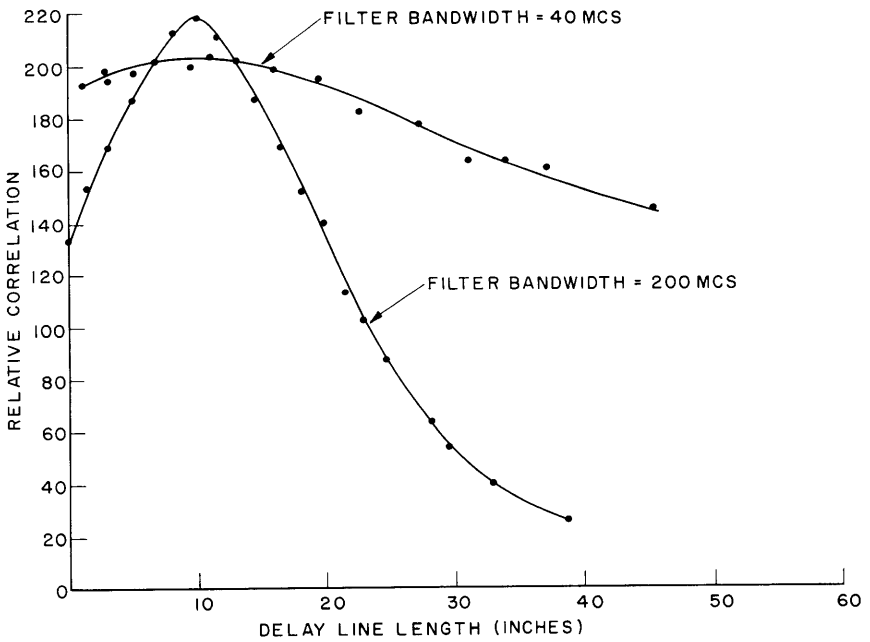

Fig. X-3. Measured autocorrelation functions for white noise passed through filters.

The crosscorrelation system was tested as follows: The bremsstrahlung noise from a fluorescent tube was passed through one of several filters in turn. The power out of the filter was split into two paths through a hybrid tee and was fed into the input channels of the crosscorrelator, thereby making it into an autocorrelator. Since the autocorrelation function of the noise should simply be the Fourier transform of the magnitude squared of the filter transfer function, one can check the operation of the crosscorrelator by comparing the correlation function with the transform of the measured filter frequency characteristics. Actually, this test was made on two filters, one with a 200-mc bandwidth and the other with 40-mc bandwidth. The autocorrelation functions were merely compared with respect to the rate of drop-off with increasing τ and the theoretical rate that one would expect. These data are given in Fig. X-3.

S. Gruber

B. MAGNETOAMBIPOLAR DIFFUSION

A Master's thesis, entitled "Steady-State Diffusion Currents in a Cylindrical Magnetoambipolar Plasma," was submitted to the Department of Electrical Engineering, M. I. T., in January 1962, by Herbert B. Wollman. Partial results of his experimental measurements were published in Quarterly Progress Report No. 63 (pages 8-11).

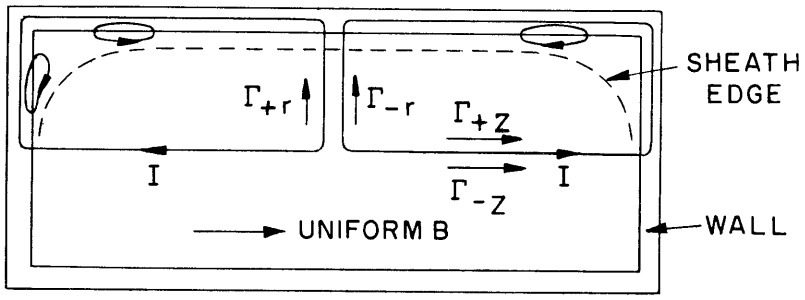

Fig. X-4. Magnetized plasma in a cylindrical cavity.

Our analysis of the problem[1] exhibits fair agreement with the results of Wollman's thesis. It has always been necessary, however, to assume that the density distribution in a cylindrical cavity with conducting walls is in its lowest mode. The theoretical proof of this fact has now been completed and is presented in this report.

The steady-state transport and conservation equations of ions and electrons in the cylindrical cavity of Fig. X-4 with a uniform magnetic field along its axis are:

$$\Gamma_{\pm z} = -D_{\pm} \frac{\partial n}{\partial z} \mp n\mu_{\pm} \frac{\partial \phi}{\partial z} \tag{1}$$

$$\Gamma_{\pm r} = -b_{\pm} D_{\pm} \frac{\partial n}{\partial r} \mp n b_{\pm} \mu_{\pm} \frac{\partial \phi}{\partial r} \tag{2}$$

$$\overline{\nabla} \cdot \overline{\Gamma}_{\pm} = n\nu_i, \tag{3}$$

where $\Gamma_{\pm z}$ and $\Gamma_{\pm r}$ are the axial and radial current densities of the ion and electron, n is the electron or ion density which are set equal, ϕ is the electrostatic potential, $D_{\pm}$ and $\mu_{\pm}$ are the diffusion and mobility coefficients, ν_i is the electron ionization frequency assumed to be constant throughout the cavity, and $b_{\pm}$ are the ion and electron "magnetic quenching factors" given by

$$b_{\pm} = \frac{1}{1 + \mu_{\pm}^2 B^2} . \tag{4}$$

In this system of six equations, there are six unknowns, $\Gamma_{\pm z}$, $\Gamma_{\pm r}$, n, and ϕ, and,

although we are assured of a solution, the equations are nonlinear because of the mobility terms. It is possible to eliminate the nonlinear terms from (1) and (2), and, by so doing, we get

$$\frac{\Gamma_{+z}}{\mu_+} + \frac{\Gamma_{-z}}{\mu_-} = -(T_+ + T_-)\frac{\partial n}{\partial z} \tag{5}$$

$$\frac{\Gamma_{+r}}{b_+\mu_+} + \frac{\Gamma_{-r}}{b_-\mu_-} = -(T_+ + T_-)\frac{\partial n}{\partial r} . \tag{6}$$

Equations 3, 5, and 6 now represent a system of four linear equations, but, unfortunately, there are five unknowns.

If we now assume that the walls of the cavity in Fig. X-4 are insulating, then the congruence condition applies, namely $\Gamma_{+r} = \Gamma_{-r}$ and $\Gamma_{+z} = \Gamma_{-z}$. With these two additional equations our solution is determined, and the equation for the density n is an eigenvalue problem when the density is set equal to zero at the walls, that is,

$$n = \sum_{k\ell} n_{k\ell} J_o(r/\Lambda_k) \cos(z/\Lambda_\ell), \tag{7}$$

where $\Lambda_k = R/a_k$, with a_k the zeros of J_o; and $\Lambda_\ell = L/\ell\pi$, with ℓ odd. The condition for any of these modes to exist in the steady state is

$$\frac{\nu_i}{D_a} - \frac{b_a}{\Lambda_k^2} - \frac{1}{\Lambda_\ell^2} = 0 \quad \text{with} \quad b_a = \frac{1}{1 + \mu_+\mu_- B^2} \tag{8}$$

and, since ν_i can have only one value, only one mode exists for the lowest value of ν_i, namely n_{11}. This result is well known.

If, however, we make the cavity walls conducting, the congruence condition is no longer true, and the ion and electron currents may be vastly different. The best that one can do with Eqs. 3, 5, and 6 is to make a harmonic analysis of the density and currents. Thus the density can again be written as a sum of modes, as in Eq. 7. The currents are then given by

$$\Gamma_{\pm z} = \sum_{k\ell} \Gamma_{\pm z, k\ell} J_o(r/\Lambda_k) \sin(z/\Lambda_\ell), \quad \Gamma_{\pm r} = \sum_{k\ell} \Gamma_{\pm r, k\ell} J_1(r/\Lambda_k) \cos(z/\Lambda_\ell) \tag{9}$$

with

$$\frac{\Gamma_{\pm z, k\ell}}{n_{k\ell}\Lambda_\ell D_a} = \frac{1}{\Lambda_\ell^2} - \frac{b_\mp}{b_a - b_\mp}\left[\frac{\nu_i}{D_a} - \frac{b_a}{\Lambda_k^2} - \frac{1}{\Lambda_\ell^2}\right] \tag{10}$$

$$\frac{\Gamma_{\pm r, k\ell}}{n_{k\ell}\Lambda_k D_a} = \frac{b_a}{\Lambda_k^2} + \frac{b_a}{b_a - b_\mp}\left[\frac{\nu_i}{D_a} - \frac{b_a}{\Lambda_k^2} - \frac{1}{\Lambda_\ell^2}\right]. \tag{11}$$

It is clear that ν_i can now have a range of values and, in addition, the higher modes may exist simultaneously with the fundamental. The only requirement is that the total density in the plasma and the net current to the wall never become negative. Therefore the analysis, thus far, does not indicate the magnitude of the higher modes. In order to determine the values of $n_{k\ell}$, $\Gamma_{\pm r, k\ell}$, and $\Gamma_{\pm z, k\ell}$, we must substitute these back in the nonlinear equations (1) and (2) and solve for the electric field.

$$E_z = \frac{\sum_{k\ell} n_{k\ell}\left(\frac{T}{\Lambda_\ell}\right) I_{z, k\ell} J_o(r/\Lambda_k) \sin(z/\Lambda_\ell)}{\sum_{k\ell} n_{k\ell} J_o(r/\Lambda_k) \cos(z/\Lambda_\ell)} \tag{12}$$

$$E_r = \frac{\sum_{k\ell} n_{k\ell}\left(\frac{T}{\Lambda_k}\right) I_{r, k\ell} J_1(r/\Lambda_k) \cos(z/\Lambda_\ell)}{\sum_{k\ell} n_{k\ell} J_o(r/\Lambda_k) \cos(z/\Lambda_\ell)} \tag{13}$$

in which $T = T_+T_-/T_+ + T_-$, and $I_{z, k\ell}$ and $I_{r, k\ell}$ are complicated expressions of $b_\pm$, $D_\pm$, Λ_k, Λ_ℓ, and ν_i.

Now there are constraints on E_z and E_r, since the cavity wall is a unipotential surface. But this surface is in contact with the sheath and not the plasma, and our solutions for the density and field are not valid in the sheath. The preceding derivation has not been for nought, however, because we must also satisfy a zero curl for the electric field:

$$\frac{\partial E_z}{\partial r} = \frac{\partial E_r}{\partial z}. \tag{14}$$

Performing these differentiations, we find that, although it is all right for any mode to exist by itself, if any two modes exist together, Eq. 14 is violated. The very important conclusion, therefore, is that only the lowest mode can exist in the plasma region. Because of this, it is possible to determine the required ν_i and the magnitude of the unbalanced currents.

We can now conclude that, in addition to the unbalanced currents that cause a current flow from the radial wall to the axial wall and back through the plasma, as shown in Fig. X-4, there will be other currents that flow in the walls and return through the

sheaths. These currents arise because the sheath voltage drop must adjust itself to a unipotential surface. The analysis of these sheath currents is difficult but will be attempted.

D. R. Whitehouse

References

1. D. R. Whitehouse, Magnetoambipolar diffusion, Quarterly Progress Report No. 57, Research Laboratory of Electronics, M.I.T., April 15, 1960, pp. 20-23.

C. THE WAKE OF A CHARGED PARTICLE MOVING THROUGH A PLASMA WITH MAGNETIC FIELD

A charged particle moving in a plasma will have both short- and long-range interaction with the surrounding medium. For a low-density plasma, the long-range Coulomb force is of major importance and causes a certain charge distribution to develop in the plasma surrounding the moving particle. For a field-free plasma, and with the ions at rest, this situation has been discussed by Bohm and Pines,[1] Akhiezer and Sitenko,[2] and and Majumdar.[3] In this report a similar investigation is presented for a plasma with a magnetic field.

Following Majumdar,[3] we shall represent the plasma by the linearized transport equation in hydrodynamic approximation:

$$\frac{\partial \vec{v}}{\partial t} = -\frac{e}{m}\vec{E} - \frac{V^2}{n_o}\vec{\nabla}n - \frac{e}{mc}\vec{v}\times\vec{H}_o, \tag{1}$$

where $\vec{H}_o$ is the constant magnetic field along the z-direction, n and $\vec{E}$ are the perturbations of electron density and macroscopic field in the plasma, n_o is the average density, $\vec{v}$ is the perturbation in the plasma electron velocity, and V is the average thermal velocity of the electrons.

The field quantities that are due to a test particle of charge q and velocity $\vec{V}_o$ in the z-direction are given by Maxwell's equations:

$$\vec{\nabla}\times\vec{E} = -\frac{1}{c}\frac{\partial \vec{H}}{\partial t} \tag{2}$$

$$\vec{\nabla}\times\vec{H} = \frac{1}{c}\frac{\partial \vec{E}}{\partial t} - \frac{4\pi}{c}n_o e\vec{v} + \frac{4\pi}{c}q\vec{V}_o\delta(\vec{r}-\vec{V}_o t) \tag{3}$$

$$\vec{\nabla}\cdot\vec{E} = -4\pi ne + 4\pi q\delta(\vec{r}-\vec{V}_o t) \tag{4}$$

$$\vec{\nabla}\cdot\vec{H} = 0. \tag{5}$$

A Fourier analysis of Eqs. 1-5 gives the following expression for the total charge

density developed:

$$\rho(\vec{r},t) = \frac{q\omega_p^2}{8\pi^3}\int \frac{e^{i\vec{k}\cdot(\vec{r}-\vec{V}_o t)}}{f(\vec{k})}\, d\vec{k} \tag{6}$$

where

$$f(\vec{k}) = \frac{\left(k^2V^2+\omega_p^2-\omega^2\right)\left[\left(k^2c^2+\omega_p^2-\omega^2\right)^2 - \omega_c^2\left(\omega-\frac{c^2k^2}{\omega}\right)\left(\omega-\frac{c^2k_z^2}{\omega}\right)\right] - \omega_c^2(\omega^2-c^2k^2)\,k_\rho^2(c^2-V^2)}{\left(k^2c^2+\omega_p^2-\omega^2\right)^2 - \omega_c^2\left(\omega-\frac{c^2k^2}{\omega}\right)\left(\omega-\frac{c^2k_z^2}{\omega}\right)}. \tag{7}$$

In (7),

$$\omega \equiv \vec{k}\cdot\vec{V}_o \tag{8}$$

is the circular frequency of the Fourier transform ρ_k of the density, k_z and k_ρ are the components of propagation vector $\vec{k}$ along and at right angles to the z-direction, ω_p and ω_c are the usual plasma and the cyclotron frequencies, $f(\vec{k}) = 0$ gives the dispersion relation of the disturbance in the plasma, which has been discussed by Allis.[4]

Following Koster,[5] we evaluate the integral in (6) by the saddle-point method, assuming large values of the quantity $\vec{R} = \vec{r} - \vec{V}_o t$. The result is

$$\rho = -\frac{q\omega_p^2}{2\pi}\frac{e^{i\vec{k}_o\cdot\vec{R}}}{|\vec{R}|}\frac{1}{\left[\frac{\partial^2 f(\vec{k}_o)}{\partial\kappa_2^2}\,\frac{\partial^2 f(\vec{k}_o)}{\partial\kappa_3^2}\right]^{1/2}}. \tag{9}$$

In (9), $\vec{k}_o$ is the solution of $f(\vec{k}) = 0$, and Eq. 8 and its value determine the saddle point, and κ_2 and κ_3 are the two components of the vector $\vec{\kappa} = \vec{k} - \vec{k}_o$ which measures the deviation of $\vec{k}$ from the saddle point. These components lie in a plane that is tangent to the surface $f(\vec{k}) = 0$, at the point $\vec{k} = \vec{k}_o$. The condition for the right-hand side of (9) to be nonzero is that the vector $\vec{R}$ should be antiparallel to the normal $\vec{\nabla}f(\vec{k}_o)$ at the point $\vec{k}_o$ on the surface $f(\vec{k}_o) = 0$.

$$\vec{R} \text{ is antiparallel to } \vec{\nabla}f(\vec{k}_o). \tag{10}$$

This last condition determines the shape of the charge-density distribution, and the solution of $f(\vec{k}) = 0$ determines the type of charge-density wave that will be set up in the medium.

Now, $f(\vec{k}) = 0$ is a bicubic equation in $\vec{k}$. It is solved by assuming that the velocity

$\vec{V}_o$ is small compared with the velocity of light c, and by neglecting ω_p^2 as compared with k^2c^2. The last assumption means that the wavelength of the disturbance must be much less than c/ω_p. As c/ω_p is much greater than the Debye length V/ω_p, this approximation excludes only very long wavelengths from our consideration.

With these assumptions, detailed examination of the equation $f(\vec{k}) = 0$ shows that there are three types of wave surface in a plot of k_z vs k_ρ. The first solution gives an open surface that is very similar to a hyperbola bounded by two asymptotes. This exists only for particle velocity $V_o > V$. Use of the condition (10), then, at once suggests that the whole disturbance is confined within a cone with semiangle given by $\sin^{-1}\frac{V}{V_o}$. The distribution of the charge density within this cone is calculated to be

$$\rho = -\frac{q}{4\pi}\frac{\omega_p^2}{V^2}\beta \frac{\exp i\left[\frac{\omega_p}{V}\left(R_z^2\beta^2 - R_\rho^2\right)^{1/2}\left(\frac{R_z^2\beta^4 + \frac{\omega_p^2+\omega_c^2}{\omega_p^2}R_\rho^2}{R_z^2\beta^4 + R_\rho^2}\right)^{1/2}\right]}{[D]\left(R_z^2\beta^2 - R_\rho^2\right)^{1/2}} \tag{11}$$

where

$$\beta = \frac{V}{\left(V_o^2 - V^2\right)^{1/2}}$$

and

$$[D] = \left[1 + \frac{\omega_c^2}{\omega_p^2}\frac{R_z^2\beta^2 - R_\rho^2}{R_z^2\beta^4 + \frac{\omega_p^2+\omega_c^2}{\omega_p^2}R_\rho^2}\cdot\frac{R_z^2\beta^4}{R_z^2\beta^4 + R_\rho^2}\right]^{1/2}$$

$$\times\left[1 - \frac{\omega_c^2}{\omega_p^2}\frac{V_o^2}{V^2}\frac{\beta^4R_z^2R_\rho^2}{\left(R_z^2\beta^4+R_\rho^2\right)^2}\cdot\frac{\frac{3V_o^2-2V^2}{V_o^2-V^2}\beta^4R_z^2 - \frac{V_o^2+2V^2}{V_o^2-V^2}R_\rho^2}{R_z^2\beta^4 + \frac{\omega_p^2+\omega_c^2}{\omega_p^2}R_\rho^2}\right]^{1/2}.$$

The quantities R_z and R_ρ are the components of $\vec{R}$, and are shown in Fig. X-5. Therefore this is a shock wave confined within a Mach cone behind the moving particle.

The second solution gives an elliptical wave with the moving particle at its center:

$$\rho = -\frac{q}{4\pi}\frac{\omega_p^2}{V^2}\delta\,\frac{\exp i\frac{\omega_c}{V_o}\sqrt{R_z^2 + R_\rho^2\frac{V_o^2}{V^2}\frac{\omega_p^2}{\omega_c^2}\delta}}{\left(R_z^2 + R_\rho^2\frac{\omega_p^2}{\omega_c^2}\frac{V_o^2}{V^2}\delta\right)^{1/2}} \tag{12}$$

where

$$2\delta = -\left(1 + \frac{\omega_c^2}{\omega_p^2}\frac{V_o^2 - V^2}{V_o^2}\right) + \sqrt{\left(1 + \frac{\omega_c^2}{\omega_p^2}\frac{V_o^2 - V^2}{V_o^2}\right)^2 + 4\frac{V^2}{V_o^2}\frac{\omega_c^2}{\omega_p^2}}.$$

This is also a radiated wave from the moving particle, existing for both $V_o >$ and $< V$. It

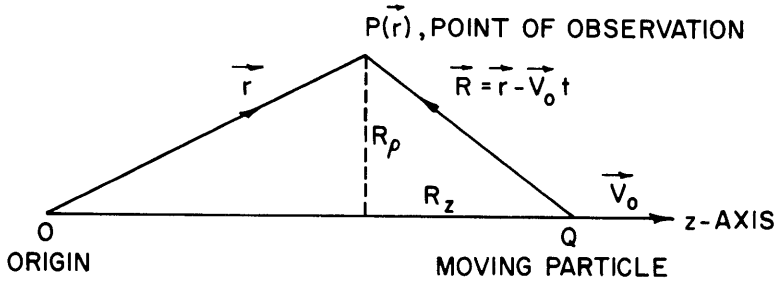

Fig. X-5. Diagram showing the point of observation with respect to the moving particle.

vanishes when ω_c goes to zero.

The third solution gives a spherical wave for large values of ω_c:

$$\rho = -\frac{q\omega_p^2}{4\pi c^2}\frac{\omega_p^2}{\omega_c^2}\frac{V_o^2}{c^2}\frac{\exp i\left[\frac{\omega_p}{\omega_c}\frac{V_o}{c}\frac{\omega_p}{c}|\vec{R}|\right]}{|\vec{R}|}. \tag{13}$$

If ω_c is zero, then in place of (13) we get a damped solution for ρ:

$$\rho = -\frac{q\omega_p^2}{8\pi c^2}\frac{\sqrt{2}c}{\left(2c^2 - V_o^2\right)^{1/2}}\frac{\exp\left[-\frac{\omega_p}{\sqrt{2}c}\left\{R_z^2\frac{2c^2}{2c^2 - V_o^2} + R_\rho^2\right\}^{1/2}\right]}{\left[R_z^2\frac{2c^2}{2c^2 - V_o^2} + R_\rho^2\right]^{1/2}}. \tag{14}$$

This is also elliptical in shape, surrounds the moving particle, and is almost identical with the transverse disturbance in the field-free plasma,[3] the slight difference arising from the neglect of ω^2 compared with k^2c^2.

S. K. Majumdar
(Alfred P. Sloan Postdoctoral Fellow)

References

1. D. Pines and D. Bohm, A collective description of electron interactions. II. Collective vs individual particle aspect of the interactions, Phys. Rev. 85, 338 (1952).

2. A. I. Akhiezer and A. G. Sitenko, Penetration of Charged Particles Through an Electron Plasma, A.E.R.E. Lib/Trans 759, Harwell (1956).

3. S. K. Majumdar, Electrodynamics of a charged particle moving through a plasma without magnetic field, Proc. Phys. Soc. (London) 76, 657 (1960).

4. W. P. Allis, Propagation of waves in a plasma in a magnetic field, Trans. IRE, Vol. MTT-9, p. 79, 1961.

5. G. F. Koster, Theory of scattering in solids, Phys. Rev. 95, 1436 (1954).

D. DETERMINATION OF ELECTRON ENERGIES AND ENERGY DISTRIBUTIONS FROM MEASUREMENTS OF THE NONTHERMAL RADIATION FROM PLASMAS

In a previous report[1] we described measurements of the ratio of emission to the absorption coefficient j_ω/a_ω from a plasma. Measurements of the departure of this ratio from the Kirchhoff-Planck law,

$$\frac{j_\omega}{a_\omega} = \frac{\omega^2}{8\pi^3 c^2}\, kT, \tag{1}$$

afford a convenient method of estimating the mean electron energy and the distribution of electron velocities in a plasma. When the plasma is not in thermodynamic equilibrium (that is, when Eq. 1 does not hold) we may write the ratio of emission to absorption symbolically as

$$\frac{j_\omega}{a_\omega} = \frac{\omega^2}{8\pi^3 c^2}\, kT_r. \tag{2}$$

Here, T_r is a fictitious temperature unless the distribution is Maxwellian, in which case T_r equals the electron temperature T. In all other cases T_r is a function of the radiation processes, the frequency, and the distribution function.

Calculations have shown that in a plasma with nonrelativistic energies, in which collisions with neutrals predominate, the radiation temperature is given by

$$kT_r = -\frac{\int_0^\infty \frac{\nu(v)}{(\omega-\omega_b)^2+\nu^2(v)} f(v)\, v^4 dv}{\int_0^\infty \frac{\nu(v)}{(\omega-\omega_b)^2+\nu^2(v)} \frac{\partial f}{\partial u}\, v^4 dv}. \tag{3}$$

Here, u is the electron energy $mv^2/2$, f(v) is the distribution function assumed to be isotropic, and $\nu(v)$ is the collision frequency for momentum transfer of an electron with neutral atoms or molecules. The quantity ω_b is the electron-cyclotron frequency of the plasma electrons that are acted upon by an external magnetic field of strength equal to $\omega_b m/e$. Equation 3 holds only for tenuous plasmas whose refractive index is close to unity. More specifically, the conditions for the applicability of Eq. 3 are:

$$\begin{aligned} &\frac{\omega_p^2}{\omega_b \nu} < 1 \qquad \text{at } \omega \doteqdot \omega_b \\ &\left(\frac{\omega_p}{\omega}\right)^2 \ll 1 \qquad \text{at } \omega \neq \omega_b \end{aligned} \tag{4}$$

where ω_p is the electron plasma frequency. All measurements were made in plasmas that satisfied these conditions.

It is clear from Eq. 3 that measurements of T_r as a function of ω_b and ω, together with known experimental values of $\nu(v)$, yield an integral equation for the distribution function f(v). This forms the basis of our determination of the distribution function. We were not able to invert the integral equation to arrive at the distribution function, nor is it clear that a unique solution exists.

For purposes of comparison of theory with experiment, we assumed a distribution function of the form

$$f(v) \propto \exp[-bv^\ell], \tag{5}$$

where

$$\int_0^\infty f(v)\, 4\pi v^2 dv = 1 \tag{6}$$

and

$$\bar{u} = \int_0^\infty \frac{mv^2}{2} f(v)\, 4\pi v^2 dv. \tag{7}$$

Here, b and ℓ are arbitrary parameters, and $\bar{u}$ is the mean electron energy. We determine b and ℓ by comparison of the calculated with the measured radiation

temperatures. Knowing b and ℓ, we find $\bar{u}$ from Eq. 7.

The form of the distribution function given by Eq. 5 holds for plasmas of low degree of ionization, where (a) elastic collisions of electrons with neutrals predominate over inelastic collisions and (b) the dc electric field is parallel to the dc magnetic field.

The distribution function depends on the applied electric fields and on the collision processes in the plasma. Our measurements were made on the positive column of a

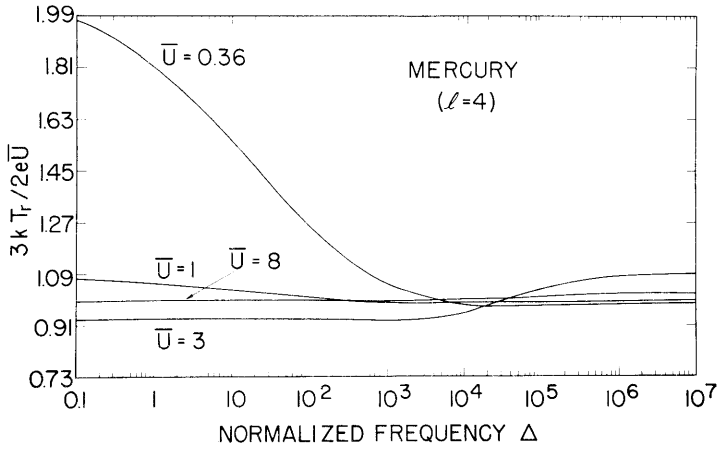

Fig. X-6. The ratio of the radiation temperature to the mean electron energy in mercury for a constant value of the distribution parameter ℓ, as a function of the normalized frequency $\Delta = \left| \frac{\omega - \omega_b}{10^2 p_o \left(\frac{2e}{m}\right)^{1/2}} \right|^2$.

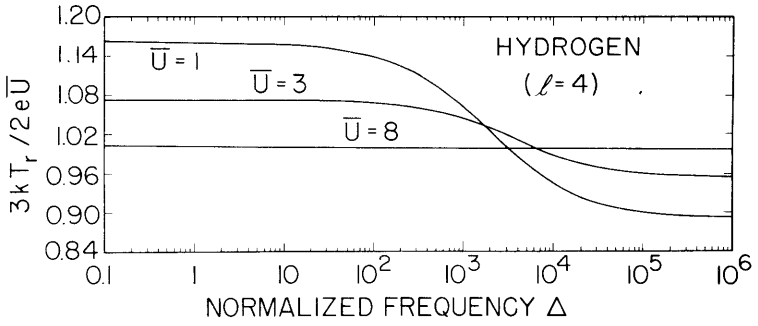

Fig. X-7. The ratio of the radiation temperature to the mean electron energy in hydrogen for a constant value of the distribution parameter ℓ, as a function of the normalized frequency $\Delta = \left| \frac{\omega - \omega_b}{10^2 p_o \left(\frac{2e}{m}\right)^{1/2}} \right|^2$.

dc discharge immersed in a magnetic field for which the criteria given above are approximately true.

The integrals of Eq. 3 were carried out numerically on a computer. In these calculations we used the previously measured results of the collision cross section for momentum transfer[2] for each gas that was studied. The calculations show that, for a

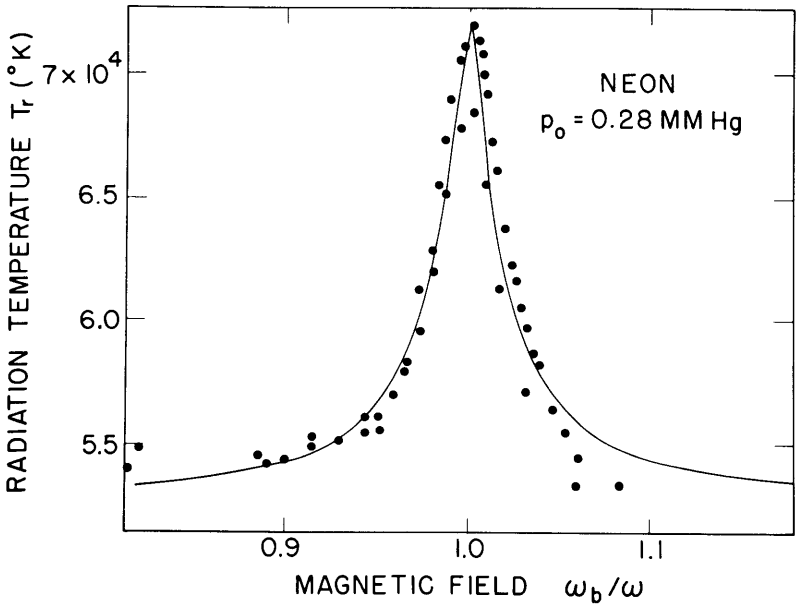

Fig. X-8. The radiation temperature as a function of the normalized magnetic field. The points are experimental values for a current of 10 ma. The theoretical curve is based on a value of $\ell = 3.4$ and of $\bar{u} = 7.75$ ev.

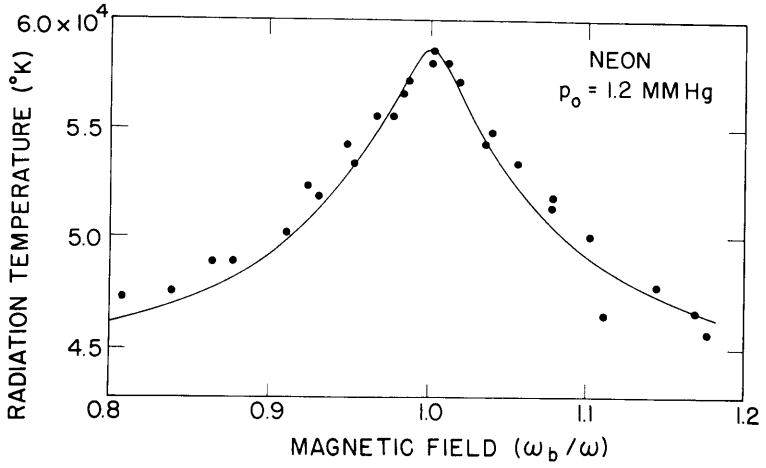

Fig. X-9. The radiation temperature as a function of the normalized magnetic field. The points are experimental values for a current of 10 ma. The theoretical curve is based on a value of $\ell = 3.3$ and of $\bar{u} = 6.35$ ev.

given departure of the plasma from thermodynamic equilibrium, the effect on the radiation temperature is most pronounced at, and close to, the electron-cyclotron frequency for gases that have a velocity-dependent ν. In the energy range for which ν is constant, T_r is invariant with frequency or magnetic field. Note from Eq. 3 that now $T_r = (2/3)(\bar{u}/k)$.

Calculations for a plasma in mercury vapor show that large peaks of the radiation

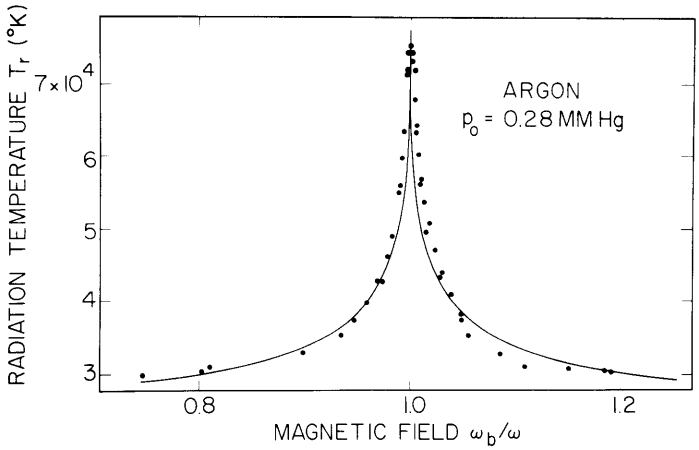

Fig. X-10. The radiation temperature as a function of the normalized magnetic field. The points are experimental values for a current of 10 ma. The theoretical curve is based on a value of $\ell = 4.13$ and of $\bar{u} = 4.55$ ev.

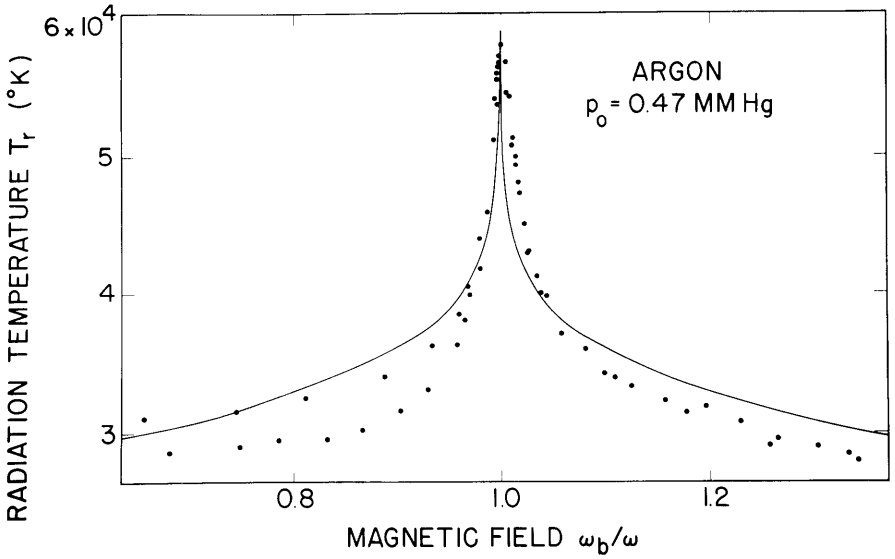

Fig. X-11. The radiation temperature as a function of the normalized magnetic field. The points are experimental values for a current of 10 ma. The theoretical curve is based on a value of $\ell = 3.02$ and of $\bar{u} = 4.52$ ev.

temperature at cyclotron resonance are to be expected at low electron energies (where ν is a steeply increasing function of v) but that hardly any peak occurs at the higher energies for which ν is approximately constant. Figure X-6 shows these calculations for one distribution function $\ell = 4$. Our experiments in mercury support these results. The mean electron energies were such that no peaks or valleys in T_r were found.

Calculations for hydrogen, Fig. X-7, show similar results. A peak in the radiation temperature at cyclotron resonance is indicated at energies below 2 ev, but no significant peak is indicated above this value. Experiments in hydrogen confirmed these results.

In neon, for which ν is approximately proportional to v, a peak is to be expected. We observed the peak at various pressures. Figures X-8 and X-9 show comparisons of experiment and theory for two gas pressures.

In argon, for which ν rises steeply with v, we find peaks larger than those in neon. Figures X-10 and X-11 show comparisons of experiment and theory for this gas.

The theoretical curves that we use in these comparisons of theory and experiment were obtained by varying b and ℓ in Eqs. 3 and 5 until the best fit to the experimental results was obtained.

In Fig. X-12 we show a plot of ℓ and the mean energy $\bar{u}$ in neon for a range of gas pressures from 0.1 to 3 mm Hg. Note that the distribution function as given by the parameter ℓ does not vary in this pressure range; on the other hand, $\bar{u}$ decreases with increasing pressure, which is in agreement with the behavior of the positive column.

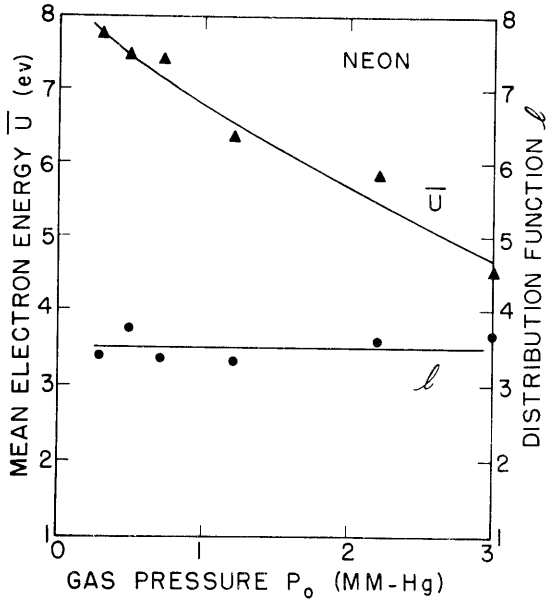

Fig. X-12. The variation of the distribution parameter ℓ, and the mean electron energy with pressure.

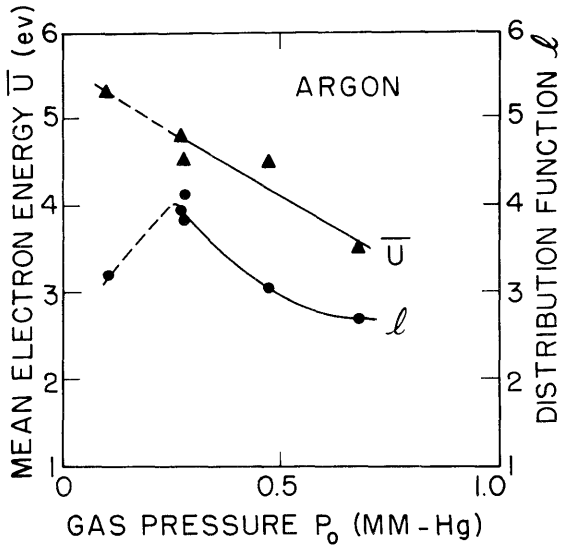

Fig. X-13. The variation of the distribution parameter ℓ, and the mean electron energy with pressure.

A similar plot for argon is shown in Fig. X-13. Here, ℓ varies significantly over the pressure range investigated, possibly because of the strong energy dependence of the collision frequency.

H. Fields, G. Bekefi

(Mr. Harvey Fields is from Microwave Associates, Burlington, Massachusetts.)

References

1. H. Fields and G. Bekefi, Microwave measurements of the radiation temperature of a plasma in a magnetic field, Quarterly Progress Report No. 62, Research Laboratory of Electronics, M.I.T., July 15, 1961, pp. 7-14.

2. S. C. Brown, Basic Data of Plasma Physics (The Technology Press of Massachusetts Institute of Technology, Cambridge, Mass., and John Wiley and Sons, Inc., New York, 1959).

E. HOLLOW-CATHODE ARC

A hollow-cathode gas-arc apparatus similar to those described previously by Getty[1] and by Rose et al.[2,3] has been constructed. The vacuum system is diagrammed in Fig. X-14. O-ring seals are used throughout, and the ultimate vacuum is from 2 to 10×10^{-7} mm Hg. The 6-inch gate valves and roughing-line valve permit the opening of the arc chamber to the atmosphere and re-evacuating it without shutting off the pumps. The arc chamber outside diameter is 6 inches and it has a 0.125-inch stainless-steel wall with six 4-inch and four 0.75-inch viewing ports. The left (cathode) and right (anode)

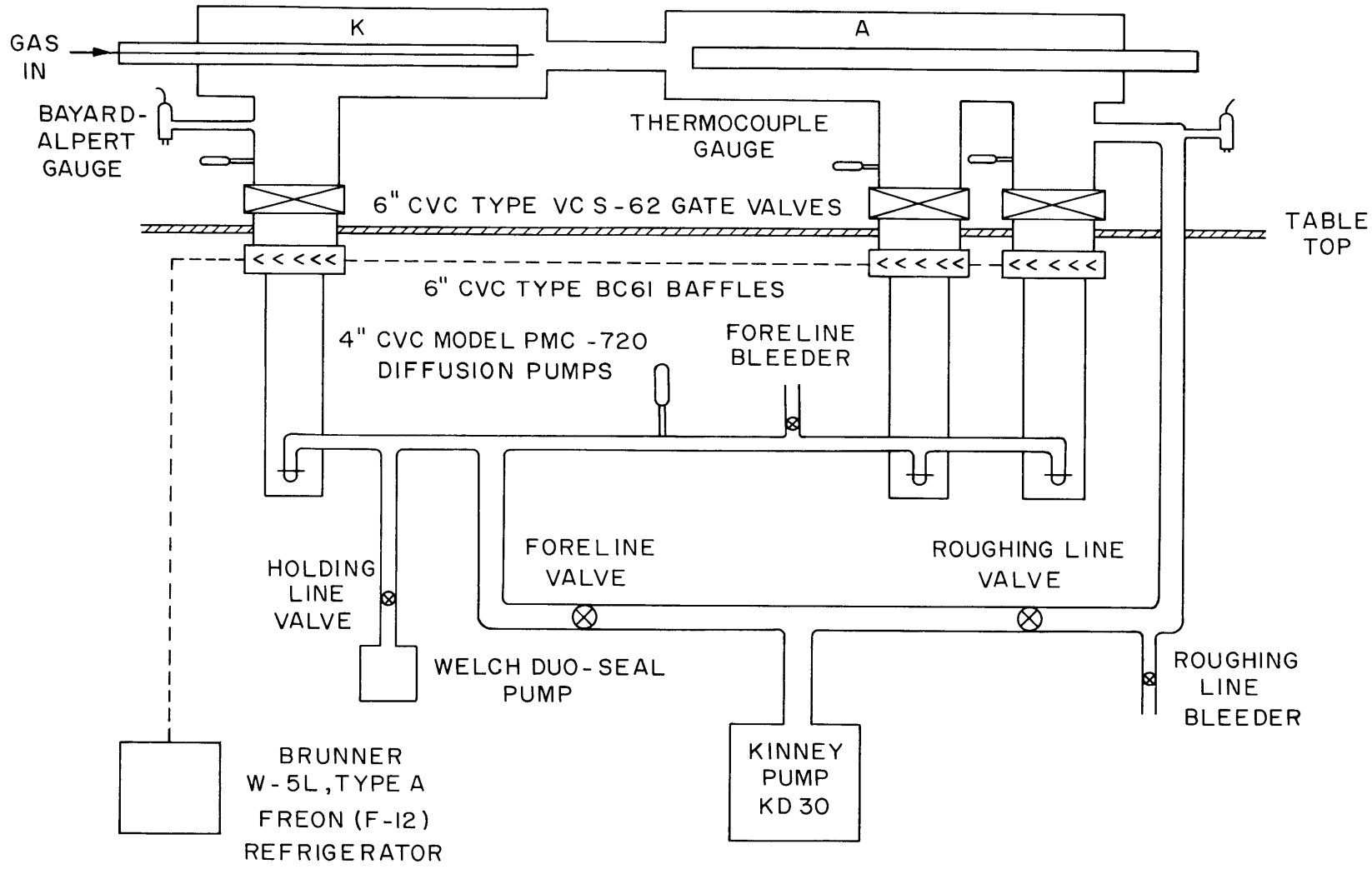

Fig. X-14. Vacuum system layout for the hollow-cathode arc.

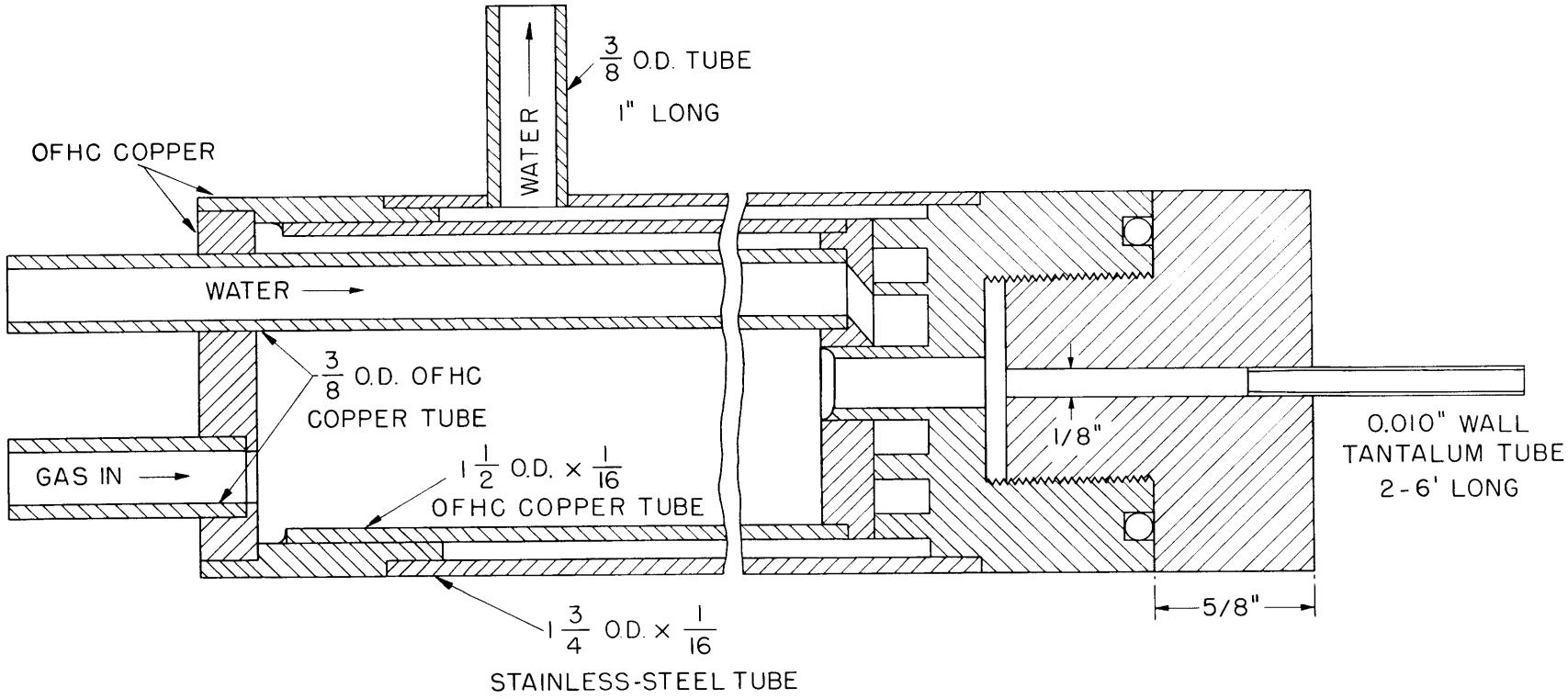

Fig. X-15. Cathode assembly.

chambers are connected by a 75-mm O.D., 9-inch-long Pyrex tube through which the arc column passes. The flanges to this section are water-cooled to protect the O-ring seals. The over-all length is 63 inches, and the arc length is variable from 9 inches to approximately 60 inches.

A pair of movable Helmholtz coils provides a magnetic field up to 2000 gauss which is uniform over 4 inches along the axis of the glass section. Two auxiliary coils capable of providing a 400-gauss field are located around the anode chamber.

Figure X-15 shows the design of the cathode holder and the hollow tantalum cathode. The anode is similar, except that there is no gas-inlet hole in the screw-in copper block. The gas, usually argon, is fed from the tank through a needle valve and flowmeter into the cathode holder.

The arc power is supplied by two Airco "Bumblebee" welders (Model 2DDR-224R, 0-300 amp) connected in series or parallel. An rf welder starter is used to preionize the gas in striking the arc.

When first put into operation in September 1961, the 9-inch glass section was only 30 mm in diameter. In this configuration the arc operated in a peculiar manner. It operated in two distinct modes, often with a discontinuous transition between them as current or magnetic field was varied. The "glow" mode operated at higher voltage and the plasma either filled the discharge tube in the manner of a glow-discharge positive column, or the slender, bright blue arc column broke up into a conically shaped pink glowlike plasma that filled the tube at the anode end. The base of the cone appeared to be fixed to the opening of the anode chamber and was not affected by the position of the Helmholtz coils. This mode ran at low and high arc currents at high magnetic fields, and for all arc currents at low magnetic field. The "arc" mode operated at lower voltage and the slender arc positive column terminated on the anode.

With all pumps on, the pressure measured at the throat of the right pump was much lower than that at the left pump. Throttling the right pumps to maintain approximately equal pressures at each ion gauge extended the range of the arc mode. Also, increasing gas flow rate and chamber gas pressure extended the arc-mode range.

Figure X-16 shows some typical V-I characteristics, and Fig. X-17 gives the loci of transition points for increasing arc current, with B held constant and pumps not throttled. There is a "hysteresis" effect so that the transition points occur at lower currents for decreasing arc current. The transition is either discontinuous, flickering, or continuous. With equlized pressures it was usually flickering or continuous.

Since all indications were that this two-mode operation was the result of low gas pressure in the vicinity of the anode, the tube was enlarged to 75 mm. With this tube the discharge runs in the arc mode for all currents up to at least 90 amps, the highest we have attempted thus far, for sufficiently great magnetic field (over ~300 gauss). At lower B fields, the glow mode runs at all currents up to at least 60 amps, the highest

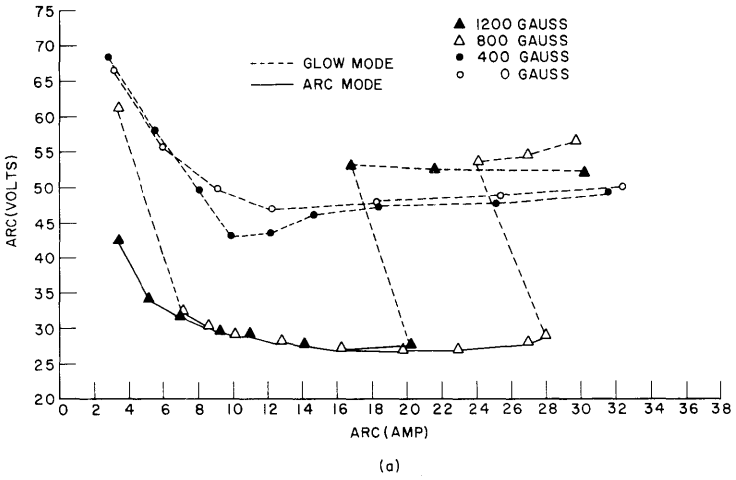

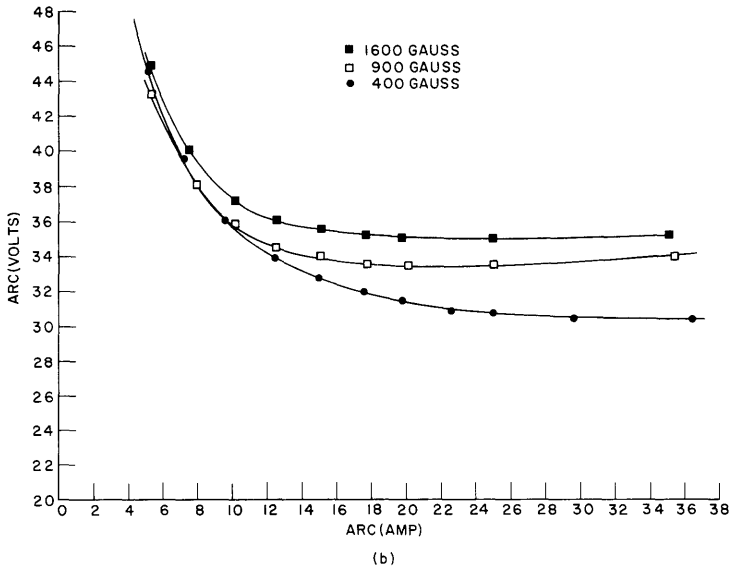

Fig. X-16. V-I characteristics (30-mm discharge tube). (a) Flow, ~65 cc-atm/min – argon; arc length, 11.5 inches; cathode chamber pressure, ~0.4μ; anode chamber pressure ~.01μ. (b) Flow, ~130 cc-atm/min; arc length, 12 inches; anode pumps throttled to maintain pressure roughly constant, 2μ.

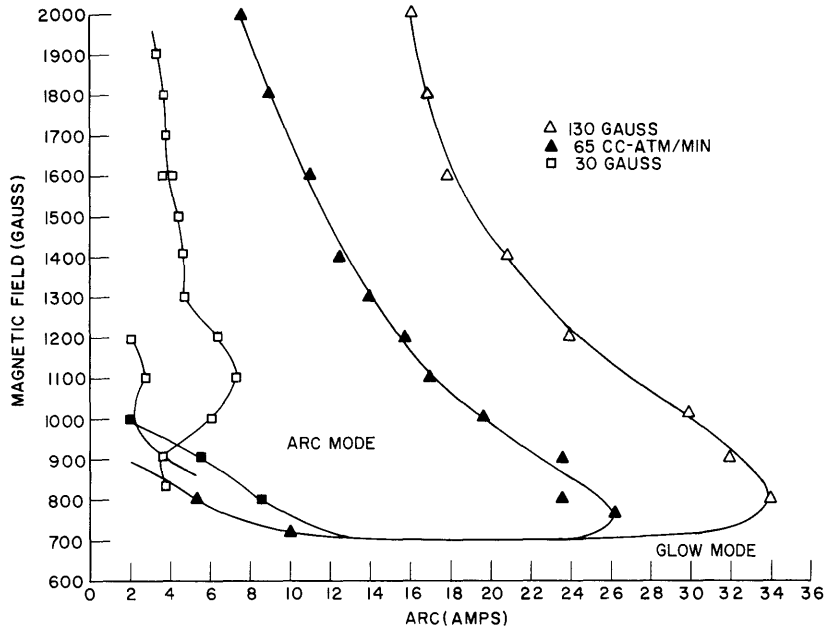

Fig. X-17. Mode transition contour (30-mm discharge tube; all pumps wide open, arc length, 11.5 inches; magnetic field held constant and arc current increased).

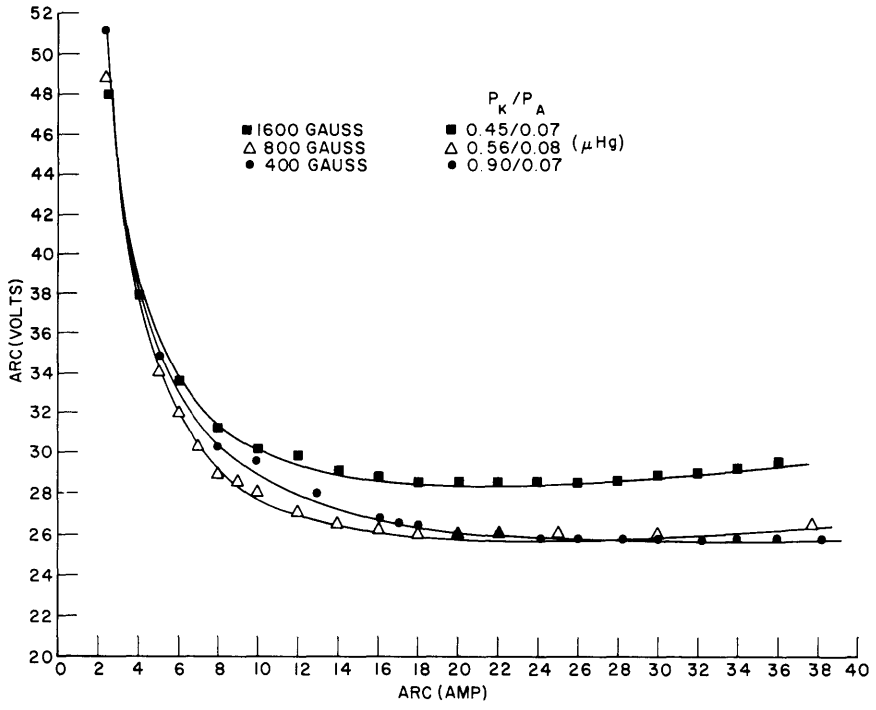

Fig. X-18. V-I characteristics: flow, 50-130 cc-atm/min; arc length, 15 inches; tube diameter, 75 mm; pumps open.

attempted in this mode. The pressure in the anode chamber is still lower than in the cathode chamber, but higher than it was with the narrow tube. Figure X-18 shows typical V-I characteristics. The flow was varied during each run to keep the cathode chamber pressure P_K roughly constant. At constant flow this pressure normally increases with arc current because the arc itself is pumping toward the cathode.

Many of the dc properties of this arc plasma and the cathode mechanism have been analyzed and discussed by Rose et al.[3] We still have not carried this any further, rather preferring to use the arc as a plasma source for plasma dynamics studies. It has become apparent, however, that our knowledge of the positive-column plasma is inadequate and more measurements and a more thorough analysis of the dc properties are necessary.

The object of the plasma dynamics studies of the arc is to investigate plasma instability and plasma transport across the magnetic field. The principal experimental problem is to find a range of arc current, applied magnetic field, and flow rate or gas pressure over which there is appreciable plasma noise that indicates the presence of an instability. If the instability results in turbulent plasma motion, the spatial correlation length of the noise signals from two points in the arc should be small compared with its length.

An attempt was made to measure light fluctuations of the arc with the optical correlator employed by Gruber and Bekefi in measuring turbulence in an rf discharge in a wind tunnel.[4] The signal-to-noise ratio was too low and no correlations could be measured. Fluctuations in light intensity at 360 cps, which were caused by the power-supply ripple, could easily be seen, but higher-frequency noise was essentially all photo tube shot noise.

An 80-turn 1-mh coil was wound around the glass tube as a magnetic probe. The natural frequency of this coil and its cable was 300 kc. A 1500-ohm parallel damping resistor made its response to the amplitude of the flux change, Φ, flat (10 per cent) up to 250 kc. The spectrum of $\Phi(f)$ (proportional to average noise voltage in 10-kc band/center frequency of band) from 10 kc to 200 kc for a 15-inch long argon arc of 60 amps and flow of 120 cc-atm/min is shown in Fig. X-19a. The spectral variation with magnetic field is cross-plotted in Fig. X-19b.

In general, the noise level in all frequency intervals increased with arc current and flow, though not all at the same rate, the higher frequencies increasing faster. Also the magnetic field at which the minimum and maximum noise amplitude occur decreases with increasing current and increasing flow.

Rough correlation measurements of this noise were made with the use of two similar coils with varying spacing along the discharge axis. The ratio of minor-to-major axis C of the Lissajous ellipses of the two signals filtered to 10-kc bandwidth as a function of frequency is plotted in Fig. X-20 for a 15-inch arc at 40 amps, 120 cc-atm/min, and 800 gauss. The low-frequency range exhibits a short correlation length, whereas the

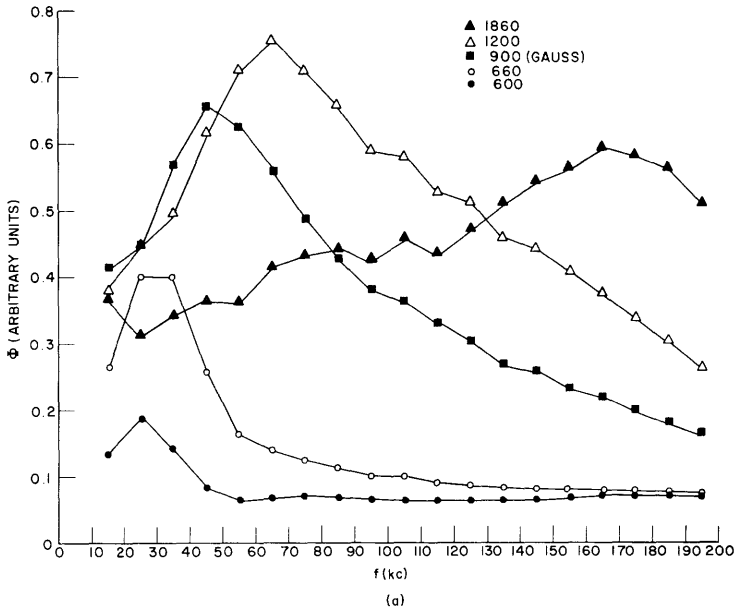

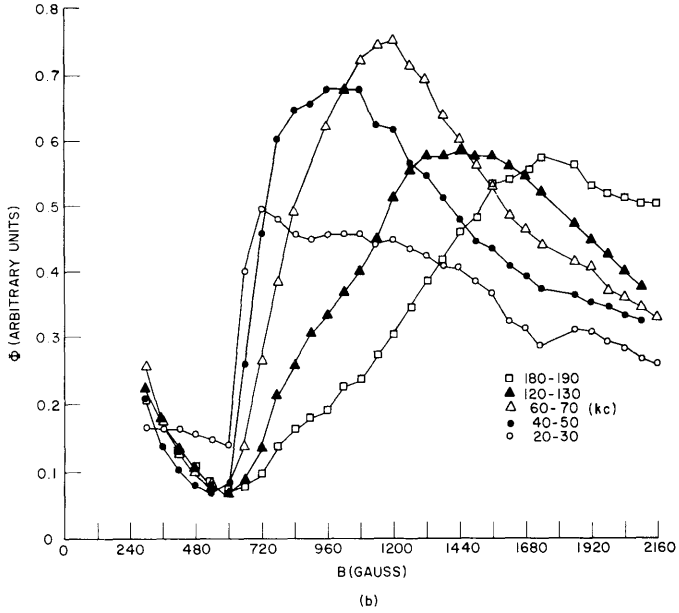

Fig. X-19. Low-frequency noise spectrum (10-kc bandwidth; arc current, 60 amps; argon flow rate ~120 cc-atm/min).

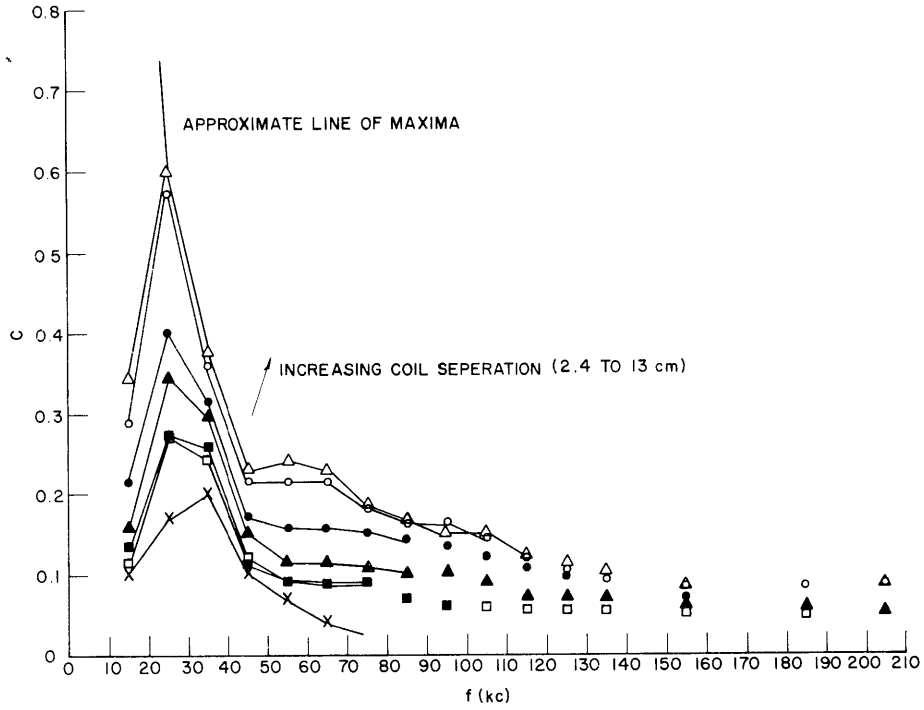

Fig. X-20. Correlator coil response. C = width/length of Lissajous figure of noise signals in 10-kc band from two pickup coils. (Arc current, 40 amps; argon flow rate ~120 cc-atm/min; magnetic field, 800 gauss.)

higher frequencies remain fairly correlated over the whole length measured. Furthermore, the Lissajous patterns at these higher frequencies appeared to have a random center and an elliptical halo that suggest that most of the width of the ellipse was due to a phase difference in the signals rather than decorrelation.

Further measurements of the spectra and correlations are necessary before we can pin down their mechanisms. They may be magnetohydrodynamic waves, ion-cyclotron oscillations, or possibly pulses of plasma (high-density striations) moving along the axis.

C. D. Buntschuh

References

1. W. D. Getty, Quarterly Progress Report No. 57, Research Laboratory of Electronics, M.I.T., April 15, 1960, pp. 27-29.

2. D. J. Rose, L. M. Lidsky, S. D. Rothleder, and S. Yoshikawa, Quarterly Progress Report No. 58, Research Laboratory of Electronics, M.I.T., July 15, 1960, pp. 41-44.

3. L. M. Lidsky, S. D. Rothleder, D. J. Rose, and S. Yoshikawa, Highly Ionized Hollow-Cathode Discharges (unpublished).

4. S. Gruber and G. Bekefi, Quarterly Progress Report No. 62, Research Laboratory of Electronics, M.I.T., July 15, 1961, pp. 14-18.